

Research Article

Detecting Damage in Thin Plates by Processing Infrared Thermographic Data with Topological Derivatives

M. Pena and M.-L. Rapún 

E.T.S.I.Aeronáutica y del Espacio, Universidad Politécnica de Madrid, Plaza Cardenal Cisneros 3, 28028 Madrid, Spain

Correspondence should be addressed to M.-L. Rapún; marialuisa.rapun@upm.es

Received 6 August 2018; Accepted 27 November 2018; Published 1 January 2019

Academic Editor: Mikhail Panfilov

Copyright © 2019 M. Pena and M.-L. Rapún. This is an open access article distributed under the Creative Commons Attribution License, which permits unrestricted use, distribution, and reproduction in any medium, provided the original work is properly cited.

A thermogram is a color image produced by a thermal camera where each color level represents a different radiation intensity (temperature). In this paper, we study the use of steady and time-harmonic thermograms for structural health monitoring of thin plates. Since conductive heat transfer is short range and the associated signal-to-noise ratio is not much favorable, efficient data processing tools are required to successfully interpret thermograms. We will process thermograms by a mathematical tool called topological derivative, showing its efficiency in very demanding situations where thermograms are highly polluted by noise, and/or when the parameters of the medium fluctuate randomly. An exhaustive gallery of numerical simulations will be presented to assess the performance and limitations of this tool.

1. Introduction

Nondestructive damage detection is a very active field for structural health monitoring of materials. In this paper, we will deal with active infrared thermography inspection, which is a technique that consists in thermally exciting (on purpose) a medium and measuring afterwards the temperature distribution in the outer surface of such medium. The temperature is recorded by using infrared cameras, which produce color images called thermograms [1] (see Figure 1 for a graphical illustration of the experimental setup). It has been used in a wide range of fields that include medical diagnosis [2, 3], aircraft [4, 5] and building [6] structural health monitoring, and night vision [7], to mention a few. Some other applications and related works can be found in [8–11].

Infrared thermography allows for recording information from the whole outer surface very fast, and it is extremely safe, more nonintrusive and noncontact than other remote testing techniques like ultrasonics [12, 13]. However, heat transport is short range and the associated signal-to-noise ratio is less favorable than in wave propagation based techniques. Moreover, infrared thermographic inspection depends on working conditions, like humidity or surrounding temperature, which

implies that it should be used in controlled environments. Due to these limitations, efficient (and rather sophisticated) data processing tools are required to successfully postprocess thermograms for structural health monitoring.

This paper is devoted to the processing of steady and time-harmonic thermograms by computing the topological derivative of the L^2 distance between the experimentally measured temperature on one side of the plate (the thermogram) and the temperature on that side when infinitesimal inclusions are located at each point of a healthy plate (simulated). This derivative can be understood as an indicator function that classifies each point of the observed region as belonging to either a defect (a cavity, crack, or inclusion) or the background medium. It is a noniterative method that does not require a priori information about the number, size, location, or shape of the unknown defects. Furthermore, it is well known that it is an extremely robust method when dealing with noise in the measured data, which makes it very appealing for industrial applications. In addition, it can also deal with noise in the medium, modeling uncertainties/fluctuations around the expected physical parameters. Topological derivative based indicator functions have been successfully tested to solve inverse problems in a wide range of fields. It is worth mentioning its usage for a

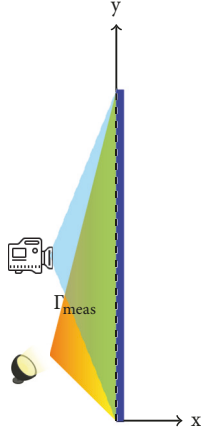


FIGURE 1: Experimental setup. The thermographic camera and the heat source (the lamp) are located at the same side of the plate. The thermogram is taken on Γ_{meas} .

two-dimensional nonsteady thermal propagation problem in a semi-infinite medium in the papers [14, 15]. A preliminary study for the setting considered in the present paper was developed in [16]. It has also been used for some related steady problems, for example, in electrical impedance tomography problems [17–19]. For related works dealing with the applicability of topological derivatives to optimal design of heat conductors, see [20, 21] and [22] for the optimization of magnetic motors. It is also worth highlighting the very recent papers [23–25] where the interested reader can find a very complete and up-to-date review about topological derivative based methods and the book [26].

In most of the papers mentioned above, authors discuss the robustness of the method with respect to noise in the measured data. However, there are very few papers where the problem of having fluctuations in the background media is taken into account. Amongst them, it is worth mentioning the works [27, 28], where the stability with respect to measurement and medium noises is analyzed for the detection of electromagnetic inclusions in an unbounded medium, and [29], devoted to an elasticity problem. In this paper, we will perform a numerical study about the stability of our topological derivative based indicator functions in terms of both measurement and medium noises. However, a theoretical justification in the spirit of the cited papers is beyond the scope of the paper and left as a possible future work.

The remainder of the paper is organized as follows. In Section 2 we formulate the direct and inverse thermal problems for the steady and time-harmonic situations. The topological derivative is introduced in Section 3, where we provide closed-form formulae for the two kinds of thermal excitations and propose a way to simultaneously process several thermograms corresponding to various locations of the lamp and/or different excitation frequencies. Section 4 is devoted to illustrate numerically the performance and limitations of the methods. Our concluding remarks are given in Section 5.

2. The Direct and Inverse Thermal Problems

The goal of this paper is to identify interior defects in a two-dimensional plate from temperature measurements (thermograms) taken on a side of a plate after heating such plate in a known and controlled manner. This is an inverse problem which is strongly ill-posed since the number, size, or location of the defects does not depend continuously on the thermograms, meaning that very slight perturbations in the data could yield a completely different set of reconstructed defects. In opposition, the direct problem consists in computing the thermogram when the location of the defects and all the internal properties are known, which is a well-posed problem, with a unique solution that depends continuously on both the defects and the parameters (small perturbations in the defects and/or in the parameters just produce small perturbations in the recorded thermogram). In this section we will formulate mathematically the direct and inverse thermal problems corresponding to steady and time-harmonic excitations.

For simplicity, we assume that the plate is rectangular and occupies the region $\Omega = [0, L_x] \times [0, L_y]$, where the width L_x is assumed to be much smaller than the height L_y (see Figure 1). The defects occupy a region $\Omega_i \subset \Omega$, which can consist in just one defect, or it can be the union of several disjoint defects. Both the direct and the inverse problems are then described by the heat equation in Ω ; namely, the temperature distribution $\mathcal{T}(\mathbf{x}, t)$ satisfies

$$\rho c \partial_t \mathcal{T} - \nabla \cdot (\kappa \nabla \mathcal{T}) = 0, \quad (1)$$

where, unless otherwise stated, the thermal parameters ρ (mass density), c (specific heat capacity), and κ (thermal conductivity) are assumed to be piecewise constant functions that attain known values inside the defects Ω_i which differ to those in the remaining of the plate $\Omega_e = \Omega \setminus \overline{\Omega}_i$. That is, in most of the paper, we assume that

$$\begin{aligned} \rho(\mathbf{x}) &= \begin{cases} \rho_i, & \mathbf{x} \in \Omega_i \\ \rho_e, & \mathbf{x} \in \Omega_e, \end{cases} \\ c(\mathbf{x}) &= \begin{cases} c_i, & \mathbf{x} \in \Omega_i \\ c_e, & \mathbf{x} \in \Omega_e, \end{cases} \\ \kappa(\mathbf{x}) &= \begin{cases} \kappa_i, & \mathbf{x} \in \Omega_i \\ \kappa_e, & \mathbf{x} \in \Omega_e, \end{cases} \end{aligned} \quad (2)$$

where $\rho_i, \rho_e, c_i, c_e, \kappa_i,$ and κ_e are positive constant values. Fluctuations in the parameters will be considered in Section 4.4, which will be modeled by adding a variation around those constant values; i.e.,

$$\tilde{\mu}(\mathbf{x}) = \begin{cases} \mu_i + \eta_\mu(\mathbf{x}), & \mathbf{x} \in \Omega_i \\ \mu_e + \eta_\mu(\mathbf{x}), & \mathbf{x} \in \Omega_e, \end{cases} \quad (3)$$

where $\tilde{\mu} = \rho, c$ or κ , and $\eta_\mu : \Omega \rightarrow \mathbb{R}$ is the random fluctuation.

We assume that the plate is isolated on its top and bottom boundaries (the shortest ones) whereas on its left and right sides heat is transferred to the surrounding air by convection and radiation. Since the temperature reached by the plate is expected to be close to the ambient temperature T_{air} , one can linearize the radiation process around T_{air} ; namely,

$$\varepsilon\sigma\mathcal{T}^4 \approx \varepsilon\sigma T_{\text{air}}^4 + 4\varepsilon\sigma T_{\text{air}}^3 (\mathcal{T} - T_{\text{air}}), \quad (4)$$

where ε and σ are the surface emissivity and the Stefan-Boltzmann constant, respectively.

The lamp will be modeled as an ideal isotropic radiator located at $\mathbf{s} = (s_x, s_y)$ with $s_x < 0$ (i.e., located at the same side of the plate where the thermogram will be taken; see Figure 1) and mathematically described in terms of the function

$$q_s(x, y) = \frac{P}{2\pi} \frac{x - s_x}{(x - s_x)^2 + (y - s_y)^2}, \quad (5)$$

where $P > 0$ corresponds to the steady radiant power of the lamp in the steady case. In the time-harmonic case, the lamp will be described as

$$\begin{aligned} q_s(x, y, t) &= \tilde{q}_s(x, y) + \Re\left(Q_s(x, y) e^{-i\omega t}\right) \\ &= \frac{\tilde{P}}{2\pi} \frac{x - s_x}{(x - s_x)^2 + (y - s_y)^2} \\ &\quad + \Re\left(\frac{P e^{-i\omega t}}{2\pi} \frac{x - s_x}{(x - s_x)^2 + (y - s_y)^2}\right), \end{aligned} \quad (6)$$

where $\omega > 0$ is the frequency of excitation, \tilde{q}_s is the steady-state contribution of a lamp of mean radiant power $\tilde{P} > 0$, and P is the complex amplitude of the radiant power harmonic oscillation.

In the time-steady case, the temperature distribution only depends on the spatial variable; i.e., $\mathcal{T}_s(\mathbf{x}, t) = T_s(\mathbf{x})$ (the subscript “s” emphasizes the dependence of the temperature on the position of the lamp) and the thermal problem is modeled by the following steady boundary value problem:

$$\begin{aligned} \nabla \cdot (\kappa_e \nabla T_s) &= 0, \quad \text{in } \Omega_e, \\ \nabla \cdot (\kappa_i \nabla T_s) &= 0, \quad \text{in } \Omega_i, \\ T_s^+ - T_s^- &= 0, \quad \text{on } \partial\Omega_i, \\ \kappa_e \partial_{\mathbf{n}} T_s^+ - \kappa_i \partial_{\mathbf{n}} T_s^- &= 0, \quad \text{on } \partial\Omega_i, \\ \partial_y T_s &= 0, \quad \text{on } y = 0, \\ \partial_y T_s &= 0, \quad \text{on } y = L_y, \\ \kappa_e \partial_x T_s - (h + 4\varepsilon\sigma T_{\text{air}}^3) T_s \\ &= -\left(hT_{\text{air}} + (\alpha + 3\varepsilon)\sigma T_{\text{air}}^4\right) - \alpha q_s, \quad \text{on } x = 0, \end{aligned}$$

$$\begin{aligned} \kappa_e \partial_x T_s + (h + 4\varepsilon\sigma T_{\text{air}}^3) T_s &= hT_{\text{air}} + (\alpha + 3\varepsilon)\sigma T_{\text{air}}^4, \\ &\text{on } x = L_x, \end{aligned} \quad (7)$$

where h is the convective heat transfer coefficient between the plate and the surrounding air and α is the absorptance of the surface. Here, the superscripts “+” and “−” appearing in the transmission conditions at the boundary of Ω_i denote limits from the exterior and the interior of Ω_i , respectively, and \mathbf{n} is the unit exterior normal vector.

In case of time-harmonic heating, after a long enough time, the temperature distribution can be modeled as $\mathcal{T}_{s,\omega}(\mathbf{x}, t) = \tilde{T}_s(\mathbf{x}) + \Re\left(T_{s,\omega}(\mathbf{x}) e^{-i\omega t}\right)$, where $\tilde{T}_s > 0$ is a steady mean value, $\omega > 0$ is the frequency of excitation, and the complex thermal amplitude $T_{s,\omega}(\mathbf{x})$, which only depends on the spatial variable \mathbf{x} , solves the stationary problem

$$\begin{aligned} \nabla \cdot (\kappa_e \nabla T_{s,\omega}) + i\omega\rho_e c_e T_{s,\omega} &= 0, \quad \text{in } \Omega_e, \\ \nabla \cdot (\kappa_i \nabla T_{s,\omega}) + i\omega\rho_i c_i T_{s,\omega} &= 0, \quad \text{in } \Omega_i, \\ T_{s,\omega}^+ - T_{s,\omega}^- &= 0, \quad \text{on } \partial\Omega_i, \\ \kappa_e \partial_{\mathbf{n}} T_{s,\omega}^+ - \kappa_i \partial_{\mathbf{n}} T_{s,\omega}^- &= 0, \quad \text{on } \partial\Omega_i, \\ \partial_y T_{s,\omega} &= 0, \quad \text{on } y = 0, \\ \partial_y T_{s,\omega} &= 0, \quad \text{on } y = L_y, \\ \kappa_e \partial_x T_{s,\omega} - (h + 4\varepsilon\sigma T_{\text{air}}^3) T_{s,\omega} &= -\alpha Q_s \quad \text{on } x = 0, \\ \kappa_e \partial_x T_{s,\omega} + (h + 4\varepsilon\sigma T_{\text{air}}^3) T_{s,\omega} &= 0, \quad \text{on } x = L_x. \end{aligned} \quad (8)$$

Notice that, comparing problem (8) with problem (7), we find the extra $i\omega\rho c$ term in the first two equations, which takes into account the time derivative in the time-harmonic case. On the other hand, the term $hT_{\text{air}} + (\alpha + 3\varepsilon)\sigma T_{\text{air}}^4$ that appears in the last two equations in (7) is not present in their counterparts in problem (8), since it and the steady heat term \tilde{q}_s (see (6)) are absorbed by the steady mean value $\tilde{T}_s(\mathbf{x})$.

The direct problem is then the following: knowing all the involved parameters, the position \mathbf{s} of the lamp, and the true defects Ω_i , solve either problem (7) or problem (8). Actual thermal cameras do not directly measure temperatures; they do measure the thermal radiation, but for solving the associated inverse problem we will assume that the actual thermogram has been already processed to contain the measured temperature distribution (in the steady case) or the measured complex thermal amplitude (in the time-harmonic one) at $x = 0$. The thermogram T^{meas} is then given by the temperature distribution at $x = 0$ (in the steady case) or by the complex thermal amplitude at $x = 0$ (in the time-harmonic one); i.e., $T_s^{\text{meas}} = T_s|_{\{x=0\}}$, with T_s solving (7) or $T_{s,\omega}^{\text{meas}} = T_{s,\omega}|_{\{x=0\}}$, with $T_{s,\omega}$ solving (8). For ease of notation, sometimes we will remove the subindexes “s” or “s, ω ”, and T^{meas} and T will be related to either problem (7) or problem (8).

The inverse problem consists in finding the defects Ω_i such that the solution T to (7) or (8) for those defects

agrees with the measured data T^{meas} at $x = 0$. From the mathematical point of view, imposing $T|_{\{x=0\}} = T^{\text{meas}}$ is a very demanding constraint taking into account that T^{meas} is expected to contain experimental errors and that this problem is strongly ill-posed. A more suitable formulation is to weaken the constraint by formulating the problem as a least squares minimization one. The new formulation consists in finding the defects Ω_i minimizing the functional

$$J_s(\Omega \setminus \overline{\Omega}_i) = \frac{1}{2} \int_{\{x=0\}} |T_s - T_s^{\text{meas}}|^2 d\ell, \quad (9)$$

where T_s is the solution to (7), in the steady case, or minimizing the functional

$$J_{s,\omega}(\Omega \setminus \overline{\Omega}_i) = \frac{1}{2} \int_{\{x=0\}} |T_{s,\omega} - T_{s,\omega}^{\text{meas}}|^2 d\ell, \quad (10)$$

with $T_{s,\omega}$ solving (8), in the time-harmonic situation.

In case of having several thermograms corresponding to several locations of the lamp in the steady case, we will consider the minimization of a linear combination of the individual functionals (9) associated with each lamp position \mathbf{s}_j ; i.e., we will consider the functional

$$J(\Omega \setminus \overline{\Omega}_i) = \sum_{j=1}^{N_{\text{lamps}}} \beta_j J_{s_j}(\Omega \setminus \overline{\Omega}_i), \quad (11)$$

where the weights $\beta_j > 0$ will balance the contribution of each individual lamp and N_{lamps} is the number of different positions of the lamp. In the time-harmonic case, we could have different thermograms resulting from different locations of the lamp and/or different excitation frequencies. In this case, we will look for a minimizer of the functional

$$J(\Omega \setminus \overline{\Omega}_i) = \sum_{j=1}^{N_{\text{lamps}}} \sum_{k=1}^{N_{\text{freq}}} \beta_{jk} J_{s_j, \omega_k}(\Omega \setminus \overline{\Omega}_i), \quad (12)$$

with J_{s_j, ω_k} defined as in (10). Here N_{lamps} is the number of positions of the lamp and N_{freq} is the number of frequencies.

The weights β_j or β_{jk} in (11) or (12) will be selected in Section 3 after computing the topological derivative of each individual functional J_{s_j} or J_{s_j, ω_k} , respectively. Indeed, they could be considered as a new set of unknowns in the minimization strategy, whose optimal selection would produce an optimal exploitation of the given thermograms. However, this extension is out of the scope of the present paper.

3. Topological Derivative

The minimization strategy to find the unknown defects Ω_i will be based on the computation of the topological derivative of the (generalized) least squares functionals. In this section, we will first define this derivative and then provide closed-form formulae for the topological derivative of the steady and time-harmonic functionals.

Let us begin with the formal definition of the topological derivative introduced in [30]. The topological derivative of a

shape functional $\mathcal{F}(\mathcal{R}) = \mathcal{F}(u_{\mathcal{R}})$, where \mathcal{R} is a domain in \mathbb{R}^2 and $u_{\mathcal{R}}$ is the solution to a given PDE problem defined in \mathcal{R} , is a scalar field D_T that measures the sensitivity of the functional when an infinitesimal ball $B_\epsilon(\mathbf{x})$ of radius ϵ is located at each point $\mathbf{x} \in \mathcal{R}$. It provides at each point $\mathbf{x} \in \mathcal{R}$ the asymptotic expansion

$$\mathcal{F}(\mathcal{R} \setminus \overline{B_\epsilon(\mathbf{x})}) = \mathcal{F}(\mathcal{R}) + D_T(\mathbf{x}) \mathcal{V}(\epsilon) + o(\mathcal{V}(\epsilon)), \quad (13)$$

as $\epsilon \rightarrow 0$,

where \mathcal{V} is a positive monotonic increasing function such that $\lim_{\epsilon \rightarrow 0^+} \mathcal{V}(\epsilon) = 0$. The function \mathcal{V} is chosen such that expansion (13) exists for all $\mathbf{x} \in \mathcal{R}$ and attains nonzero values in a nonempty set of points $\mathbf{x} \in \mathcal{R}$. In our case, we can choose $\mathcal{V}(\epsilon) = \pi\epsilon^2$, i.e., the area of the ball. Expansion (13) motivates our reconstruction technique: we will place defects in the regions where the topological derivative attains pronounced negative values; i.e., we will cluster all the points where the error functional is expected to decrease the most. This means that the true set of defects Ω_i will be approximated by the set

$$\Omega_{\text{app}} := \left\{ \mathbf{x} \in \Omega; D_T(\mathbf{x}) < \lambda \min_{\mathbf{y} \in \Omega} D_T(\mathbf{y}) \right\} \quad (14)$$

where $0 < \lambda < 1$ is a tunable threshold. Notice that the closer to one, the fewer the points. The sensitivity of the method in terms of the choice of this parameter will be tested in Section 4. It is clear that the direct numerical implementation of definition (13) is completely unfeasible from a practical point of view. To amend this problem, in the next two theorems we will provide closed-form formulae for the topological derivative of the individual functionals (9) and (10), which are well-suited for the numerical computation of set (14). These results can be derived by using the relationship between shape and topological derivatives established in [31] and performing suitable adjustments (to deal with the different boundary conditions at the sides of the plate) to the results obtained by one of us in [18] for the steady case and in [32, 33] for the time-harmonic one.

Theorem 1. *The topological derivative D_T^s of the steady cost functional J_s defined in (9) is given by*

$$D_T^s(\mathbf{x}) = \frac{2\kappa_e(\kappa_e - \kappa_i)}{\kappa_e + \kappa_i} \nabla T_s^0(\mathbf{x}) \cdot \nabla V_s^0(\mathbf{x}), \quad \mathbf{x} \in \Omega, \quad (15)$$

where T_s^0 is the solution to the problem

$$\begin{aligned} \nabla \cdot (\kappa_e \nabla T_s^0) &= 0, \quad \text{in } \Omega, \\ \partial_y T_s^0 &= 0, \quad \text{on } y = 0, \\ \partial_y T_s^0 &= 0, \quad \text{on } y = L_y, \\ \kappa_e \partial_x T_s^0 - (h + 4\epsilon \sigma T_{\text{air}}^3) T_s^0 &= 0, \\ &= -(h T_{\text{air}} + (\alpha + 3\epsilon) \sigma T_{\text{air}}^4) - \alpha q_s, \quad \text{on } x = 0, \\ \kappa_e \partial_x T_s^0 + (h + 4\epsilon \sigma T_{\text{air}}^3) T_s^0 &= h T_{\text{air}} + (\alpha + 3\epsilon) \sigma T_{\text{air}}^4, \end{aligned} \quad (16)$$

$$\text{on } x = L_x,$$

and V_s^0 solves the following associated adjoint problem:

$$\begin{aligned} \nabla \cdot (\kappa_e \nabla V_s^0) &= 0, \quad \text{in } \Omega, \\ \partial_y V_s^0 &= 0, \quad \text{on } y = 0, \\ \partial_y V_s^0 &= 0, \quad \text{on } y = L_y, \\ \kappa_e \partial_x V_s^0 - (h + 4\varepsilon\sigma T_{air}^3) V_s^0 &= T_s^{\text{meas}} - T_s^0, \quad \text{on } x = 0, \\ \kappa_e \partial_x V_s^0 + (h + 4\varepsilon\sigma T_{air}^3) V_s^0 &= 0, \quad \text{on } x = L_x. \end{aligned} \quad (17)$$

Theorem 2. The topological derivative $D_T^{s,\omega}$ of the time-harmonic cost functional $J_{s,\omega}$ defined in (10) is given by

$$\begin{aligned} D_T^{s,\omega}(\mathbf{x}) &= \Re e \left(\frac{2\kappa_e(\kappa_e - \kappa_i)}{\kappa_e + \kappa_i} \nabla T_{s,\omega}^0(\mathbf{x}) \cdot \overline{\nabla V_{s,\omega}^0(\mathbf{x})} \right. \\ &\quad \left. - i\omega(\rho_e c_e - \rho_i c_i) T_{s,\omega}^0(\mathbf{x}) \overline{V_{s,\omega}^0(\mathbf{x})} \right), \quad \mathbf{x} \in \Omega, \end{aligned} \quad (18)$$

where $T_{s,\omega}^0$ is the solution to the problem

$$\begin{aligned} \nabla \cdot (\kappa_e \nabla T_{s,\omega}^0) + i\omega\rho_e c_e T_{s,\omega}^0 &= 0, \quad \text{in } \Omega, \\ \partial_y T_{s,\omega}^0 &= 0, \quad \text{on } y = 0, \\ \partial_y T_{s,\omega}^0 &= 0, \quad \text{on } y = L_y, \\ \kappa_e \partial_x T_{s,\omega}^0 - (h + 4\varepsilon\sigma T_{air}^3) T_{s,\omega}^0 &= -\alpha Q_s, \quad \text{on } x = 0, \\ \kappa_e \partial_x T_{s,\omega}^0 + (h + 4\varepsilon\sigma T_{air}^3) T_{s,\omega}^0 &= 0, \quad \text{on } x = L_x. \end{aligned} \quad (19)$$

and $V_{s,\omega}^0$ solves the associated adjoint problem

$$\begin{aligned} \nabla \cdot (\kappa_e \nabla V_{s,\omega}^0) - i\omega\rho_e c_e V_{s,\omega}^0 &= 0, \quad \text{in } \Omega, \\ \partial_y V_{s,\omega}^0 &= 0, \quad \text{on } y = 0, \\ \partial_y V_{s,\omega}^0 &= 0, \quad \text{on } y = L_y, \\ \kappa_e \partial_x V_{s,\omega}^0 - (h + 4\varepsilon\sigma T_{air}^3) V_{s,\omega}^0 &= T_{s,\omega}^{\text{meas}} - T_{s,\omega}^0, \\ &\quad \text{on } x = 0, \\ \kappa_e \partial_x V_{s,\omega}^0 + (h + 4\varepsilon\sigma T_{air}^3) V_{s,\omega}^0 &= 0, \quad \text{on } x = L_x. \end{aligned} \quad (20)$$

Notice that the measured data T^{meas} , i.e., the thermogram, is incorporated in the topological derivative by means of the right hand side at the boundary condition on $x = 0$ in the adjoint problem (17) or (20).

It is important to highlight now that, in view of the previous theorems, the implementation of the reconstruction strategy stated in (14) is very simple from the computational point of view: one just needs to solve a direct problem and a related adjoint one, which take place in the healthy plate Ω , where no defect is present (notice that (16) and (19) are nothing but problems (7) and (8) when $\Omega_i = \emptyset$). Therefore, no information about the true number, location, size, or

shape of the unknown defects is needed. Furthermore, when dealing with steady thermograms, formula (15) only depends on the interior conductivity κ_i through the multiplying factor $2\kappa_e(\kappa_e - \kappa_i)/(\kappa_e + \kappa_i)$ (T_s^0 and V_s^0 are independent of κ_i). Since we are only interested in the most pronounced negative values of D_T^s , the actual value of κ_i is completely irrelevant, one just needs to know if $\kappa_e > \kappa_i$ or $\kappa_e < \kappa_i$. In the time-harmonic case, the dependence on the interior parameters is more subtle, since the corresponding formula (18) is a linear combination of two terms, $\nabla T_{s,\omega}^0 \cdot \overline{\nabla V_{s,\omega}^0}$ and $T_{s,\omega}^0 \overline{V_{s,\omega}^0}$, and the coefficients depend on the interior parameters. The coefficient associated with the inner product of the gradients accounts for the conductivity contrast, while the coefficient for the term $T_{s,\omega}^0 \overline{V_{s,\omega}^0}$ is related to the difference in the product of the mass density by the specific heat capacity. If the parameters κ_i , ρ_i , and c_i were unknown, one could compute the sensitivity due to the conductivity contrast, i.e., $\nabla T_{s,\omega}^0 \cdot \overline{\nabla V_{s,\omega}^0}$, and the sensitivity due to the product ρc contrast, i.e., $T_{s,\omega}^0 \overline{V_{s,\omega}^0}$, and use them as independent damage indicator functions or combine them using some normalization. For related works in electromagnetism where different topological derivative based indicator functions for only permeability or conductivity contrast are considered, see [28, 34, 35].

When multiple thermograms are available, corresponding to different locations of the lamp for the steady situation, or to different excitation frequencies and/or lamp positions in the time-harmonic case, we consider the weighted functionals (11) and (12), respectively. By linearity, the topological derivative of these functionals is nothing but the linear combination of the topological derivatives of the individual functionals. Following the ideas in [35, 36], we propose to select the weights in (11) and (12) as

$$\begin{aligned} \beta_j &= \frac{1}{\left| \min_{\mathbf{y} \in \Omega} D_T^{s_j}(\mathbf{y}) \right|}, \\ \beta_{jk} &= \frac{1}{\left| \min_{\mathbf{y} \in \Omega} D_T^{s_j, \omega_k}(\mathbf{y}) \right|}. \end{aligned} \quad (21)$$

This choice avoids neglecting the contribution of some positions of the lamp and/or some frequencies that could be disregarded by simply adding the contributions (i.e., by selecting $\beta_j = 1$ or $\beta_{jk} = 1$), since with this choice we guarantee that $\min_{\mathbf{y} \in \Omega} \beta_j D_T^{s_j}(\mathbf{y}) = -1$ and $\min_{\mathbf{y} \in \Omega} \beta_{jk} D_T^{s_j, \omega_k}(\mathbf{y}) = -1$. Of course, as already mentioned, other choices could be possible. Other examples for different indicator functions where the weights are selected either a priori or a posteriori (as we do) can be found in [37–41].

4. Numerical Experiments

In this section we briefly comment on the generation of synthetic thermograms via solving problems (7) or (8) and the implementation of the topological derivative indicator functions. After that, we present a gallery of numerical examples illustrating the performance of the topological derivative when varying the different parameters of the

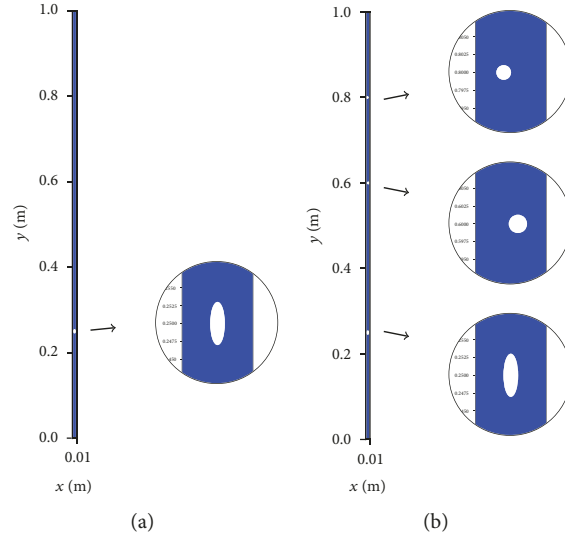


FIGURE 2: Plate Ω with dimensions $L_x = 0.01$ m and $L_y = 1$ m with different damage configurations: (a) one elliptical hole and (b) three holes of different shapes and sizes.

problem, namely, the number of defects, the positions of the lamp, the number of frequencies, and the level of noise in both the thermograms and the physical parameters.

4.1. Generation of Synthetic Thermograms and Implementation of the Topological Derivative. In case of having actual experimental thermograms (real measurements obtained by using a thermal camera), the implementation of the topological derivative only requires to solve a direct and a related adjoint problem which take place in a healthy plate, i.e., where no defects are present. However, we do not have actual thermograms, and, therefore, we need to synthetically generate them by solving numerically the direct problem (7) or (8) for the damaged plate.

For all the experiments in this section, we consider an aluminum plate of dimensions $L_x = 0.01$ m and $L_y = 1$ m, with elliptical or circular holes consisting of air. The physical parameters for these materials are $\kappa_e = 200$ W/K, $\rho_e = 2700$ Kg/m², $c_e = 900$ J/(Kg · K), $\kappa_i = 0.025$ W/K, $\rho_i = 1$ Kg/m², $c_i = 1000$ J/(Kg · K). The remaining parameters appearing in the boundary conditions are $\alpha = 0.4$, $\varepsilon = 0.08$, $h = 15$ W/(m · K), $T_{\text{air}} = 290$ K.

We will consider two different damaged plates: a plate with an elliptical hole located at $(0.5L_x, 0.25L_y)$ and semiaxes of 1 mm and 3mm and a plate with three internal holes, the same elliptical one, and two small circular ones, the first located at $(0.6L_x, 0.6L_y)$ with radius 1.25 mm and the second one located at $(0.4L_x, 0.8L_y)$ and with radius 1 mm. These plates are shown in Figure 2.

Lamps will be placed on the left hand side of the plate by considering forcing terms of the form (5), where $P = 600$ W for the steady-state case and $P = 6000$ W for the time-harmonic one. When locating the lamp at a distance 0.15 m of the plate, this kind of heating produces temperatures ranging between 300 K in the coldest parts of the plate and 303 K in the hottest ones for the steady-state case and maximum amplitudes of 0.1 K for the time-harmonic situation.

Thermograms were generated by solving numerically the corresponding direct problems (7) or (8) by using *FreeFem++* [42], which is a free integrated development environment for numerically solving partial differential equations using the finite element method. For the steady thermograms, a mesh adapted to the defects of about 24000 triangles is used with P_1 elements, while, for the time-harmonic situation, we used a finer mesh with about 53000 triangles, adjusted to the higher frequencies to be considered. These meshes generate results that are robust up to the fifth significant figure. To both prevent inverse crimes and simulate thermograms polluted by noise, after computing the synthetic thermogram T^{meas} we will always add a random noise of size $\varepsilon_{\text{err}} > 0$ to generate our noisy thermogram as

$$T^{\text{meas}, \varepsilon_{\text{err}}} = T^{\text{meas}} + \varepsilon_{\text{err}} r(y), \quad y \in [0, L_y], \quad (22)$$

where $r(y)$ is a random number with $|r(y)| \leq 1$ (real between -1 and 1 in the steady case, and complex in the time-harmonic one with real and imaginary parts between -1 and 1) generated by making use of the function `randreal1` of *FreeFem++*. Unless otherwise stated, for the steady cases we will take $\varepsilon_{\text{err}} = 0.06$, while, in the time-harmonic one, $\varepsilon_{\text{err}} = 0.01$. These values were calibrated to simulate highly polluted thermograms, since for those numbers

$$\begin{aligned} & \max_{y \in [0, L_y]} |T^{\text{meas}}(y) - T^{\text{meas}, \varepsilon_{\text{err}}}(y)| \\ & \approx 2 \max_{y \in [0, L_y]} |T^{\text{meas}}(y) - T^{\text{meas}, \text{healthy}}(y)|, \end{aligned} \quad (23)$$

where $T^{\text{meas}, \text{healthy}}$ is the thermogram corresponding to a healthy plate, without any defect.

For the implementation of the topological derivative formulae (15) and (18), we use different meshes (where the defects are not present) than for computing the thermograms, with a comparable number of triangles (20000 for the

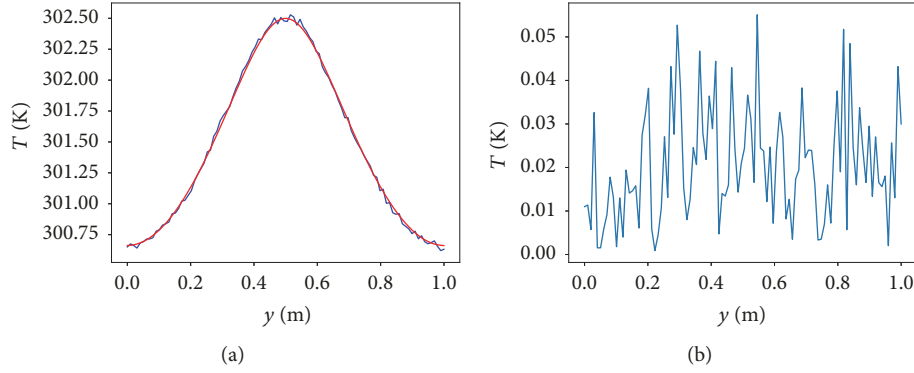


FIGURE 3: (a) Thermograms associated with a damaged (blue line) and a healthy plate (red line). (b) Absolute value of the difference between thermograms in (a).

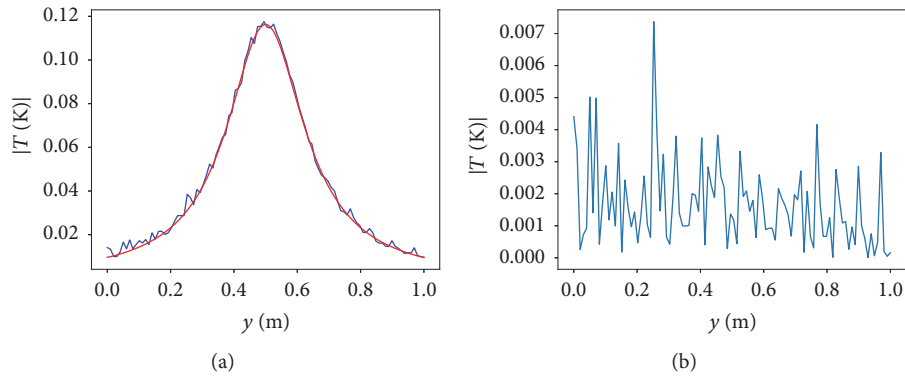


FIGURE 4: Counterpart of Figure 3 for the time-harmonic situation with $\omega = 1$ Hz.

steady case and 46000 for the time-harmonic one). Once problems (16) (or (19)) and (17) (or (20)) are solved, to implement formula (15) (or (18)), gradients are computed by using the *FreeFem++* commands to compute spatial derivatives.

For illustration, we consider the damaged plate in Figure 2(b) and locate a lamp at $(-0.15, 0.5)$, and compute the solution to the direct problem (7) at $x = 0$, and add a random perturbation of size $\varepsilon_{\text{err}} = 0.06$ to it as in (22). This produced the noisy thermogram represented in Figure 3(a) by a blue line. In case of not having any defect, by solving problem (16) we obtain the associated thermogram corresponding to a healthy plate, which is represented in Figure 3(a) by a red line. By comparing both steady thermograms, we observe that by simple inspection it is not feasible to deduce if there is damage or not, as can be checked in Figure 3(b). In the time-harmonic situation, we observe the same behavior for high levels of noise ($\varepsilon_{\text{err}} = 0.01$), as shown in Figure 4, where we have reproduced the same experiment, locating the lamp at the same position and generating a time-harmonic excitation for the frequency $\omega = 1$ Hz.

In the remaining of the section, we will illustrate the performance of the topological derivative when processing this kind of thermograms, and how they improve the results provided by just simple inspection of the thermograms. Results will be obtained by implementing the topological derivative formula for the steady case; i.e.,

$$D_T^*(\mathbf{x}) = \sum_{j=1}^{N_{\text{lamps}}} \frac{D_T^{s_j}(\mathbf{x})}{\left| \min_{\mathbf{y} \in \Omega} D_T^{s_j}(\mathbf{y}) \right|}, \quad \mathbf{x} \in \Omega, \quad (24)$$

and for the time-harmonic one

$$D_T^*(\mathbf{x}) = \sum_{j=1}^{N_{\text{lamps}}} \sum_{k=1}^{N_{\text{freq}}} \frac{D_T^{s_j, \omega_k}(\mathbf{x})}{\left| \min_{\mathbf{y} \in \Omega} D_T^{s_j, \omega_k}(\mathbf{y}) \right|}, \quad \mathbf{x} \in \Omega, \quad (25)$$

as explained above. Indeed, for an easier visualization, we will represent in the forthcoming numerical experiments the values of the normalized topological derivative

$$D_T(\mathbf{x}) = \frac{D_T^*(\mathbf{x})}{\left| \min_{\mathbf{y} \in \Omega} D_T^*(\mathbf{y}) \right|}, \quad \mathbf{x} \in \Omega, \quad (26)$$

with D_T^* defined as in (24) or (25). By doing this, we set to -1 its minimum value, and we can then define the approximated defects as the following the set of points:

$$\Omega_{\text{app}} := \{\mathbf{x} \in \Omega; D_T(\mathbf{x}) < -\lambda\}, \quad (27)$$

with $0 < \lambda < 1$.

4.2. Steady Thermograms. In this section we will test the performance of the topological derivative for the steady case. Let us begin by considering the plate with one elliptical hole,

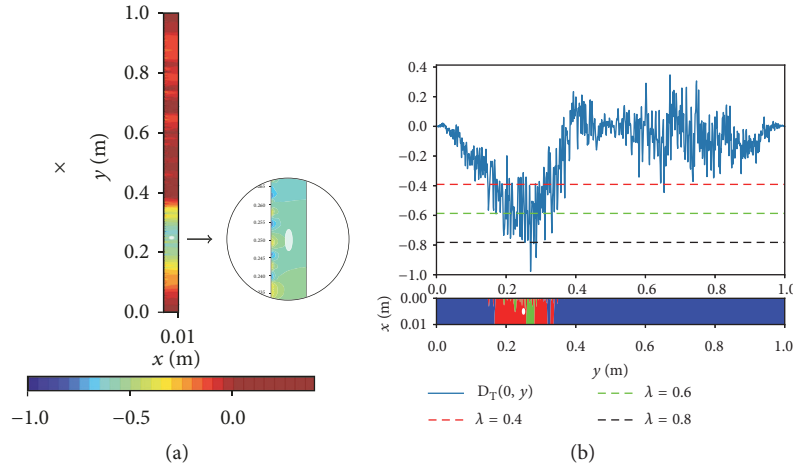


FIGURE 5: (a) Topological derivative when considering one lamp located at $(-0.15, 0.5)$, indicated by an \times -mark. (b) Topological derivative at $x = 0$ and reconstructed defects for several values of λ in (27).

represented in Figure 2(a). When processing the thermogram represented by a blue line in Figure 3(a), which corresponds to locating a lamp at $(-0.15, 0.5)$ and to a noise level $\varepsilon_{\text{err}} = 0.06$, the topological derivative (26) (for $N_{\text{lamps}} = 1$) provides the colormap represented in Figure 5(a), where the coldest colors correspond to the largest negative values, and all values above zero are represented by the same color red. We observe that the most pronounced negative values (blue and green colors) are attained in a region around the defect and that selecting $\lambda = 0.8$ in (27) we just identify a few very tiny defects, corresponding to the darkest blue colors. Notice that the scaling of the full plate in the horizontal direction, which corresponds to the interval $[0, L_x]$, is different from that in the vertical direction (corresponding to the interval $[0, L_y]$) for ease of visualization, while for the small enlarged region containing the defect the scaling is the same in both directions. For a better visualization, we represent in the upper part of Figure 5(b) the values of the topological derivative on the side $x = 0$ (blue line), where the thermogram was taken. Comparing with Figure 3, it is clear that the topological derivative has more relevant information about the presence of the defect. However, by selecting different values of λ in (27), the reconstructed defect is not sharp, as can be seen in the bottom part of Figure 5(b), where we represent the (rotated) plate, where the true defect is represented in white, and the reconstructed defects (corresponding to different values of λ) are given by different color regions. Again, the scaling of the plate in the horizontal direction, which corresponds now to the interval $[0, L_y]$, is different from that in the vertical direction (corresponding to the interval $[0, L_x]$) for ease of visualization. When selecting $\lambda = 0.8$, a few tiny regions are identified (in color black), which are not properly located and almost not seen in Figure 5(b). Decreasing this value to $\lambda = 0.6$, the reconstructed defects occupy the black and green regions, misplacing the location of the defect slightly to the center of the plate and creating some small spurious defects. Considering $\lambda = 0.4$ the reconstructed region is the union of the black, green, and red regions, which highly overestimates the size.

We want to emphasize that when dealing with thermograms that are highly corrupted by noise, the problem is very challenging, as already illustrated in Figure 3. Indeed, depending on the location of the lamp, the topological derivative can have serious difficulties to distinguish between healthy and damaged plates, or to properly identify the position of the holes in damaged plates. This is illustrated in Figure 6, where we have repeated the experiment for the same noise level, but locating the lamp at $(-0.15, 0.15)$ (Figure 6(a)) and at $(-0.15, 0.85)$ (Figure 6(b)). We observe two noteworthy features: in the first case, we detect the presence of damage, but the location of the reconstructed defect is completely wrong, while, for the second position of the lamp, the topological derivative presents an unclear minimum in the region where the defect is located, which can be misinterpreted to conclude that the plate is healthy. On the other hand, some other locations of the lamp could yield to better reconstructions than those in Figure 5.

In view of the previous results, and taking into account that we do not have information about the possible location of the defects to be used for a suitable location of the lamp, it seems reasonable to take several thermograms, corresponding to different locations of the lamp, and combine them to exploit the data. In the next experiments we process simultaneously several thermograms with a noise level $\varepsilon_{\text{err}} = 0.06$ by computing the weighted topological derivative defined by (24) and (26). First, we consider ten uniformly distributed positions (s_x, s_y) with $s_x = -0.15$, tagged in Figure 7(a) by \times -marks. Figure 7 is the counterpart of Figure 5. Now, when selecting $\lambda = 0.6$ the reconstructed region is the union of the black and the green zones, which is much closer to the true defect than when considering just one lamp, although it also contains some tiny small spurious defects located close to $y = 0.75$. This effect is better visualized by selecting $\lambda = 0.4$, which provides a reconstruction which seems to indicate that two different defects are present. The appearance of the spurious defect around $y = 0.75$ is an artifact due to the high level of noise in the thermograms. Indeed, we repeated this experiment several times by considering

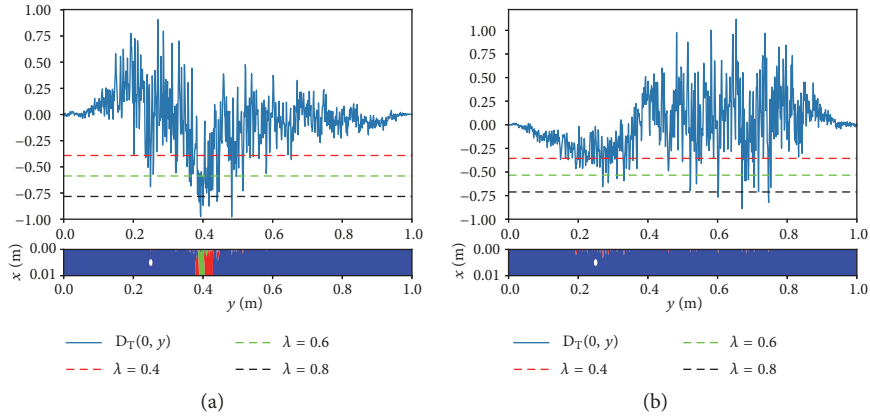


FIGURE 6: Counterpart of Figure 5(b) for different positions of the lamp. (a) Lamp at $(-0.15, 0.15)$. (b) Lamp at $(-0.15, 0.85)$.

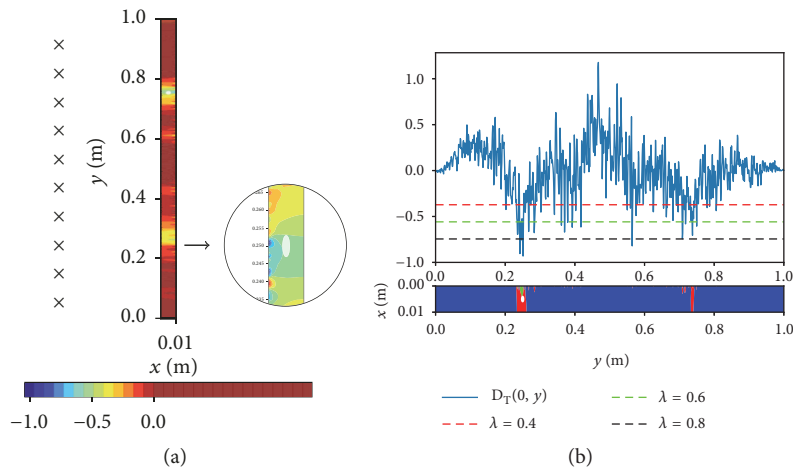


FIGURE 7: Topological derivative when considering $N_{\text{lamps}} = 10$ different locations of the lamp, indicated by \times -marks. (b) Topological derivative at $x = 0$ and reconstructed defects for several values of λ in (27).

different thermograms corresponding to the same positions of the lamp and to the same level of noise, and in some of the cases the spurious region was not found. By reducing the level of noise to $\varepsilon_{\text{err}} = 0.015$ the spurious region also disappears. Notice that, in view of (23), we can assure that, for $\varepsilon_{\text{err}} = 0.015$ and for each thermogram $T^{\text{meas}, \varepsilon_{\text{err}}}$,

$$\begin{aligned} & \max_{y \in [0, L_y]} |T^{\text{meas}}(y) - T^{\text{meas}, \varepsilon_{\text{err}}}(y)| \\ & \approx \frac{1}{2} \max_{y \in [0, L_y]} |T^{\text{meas}}(y) - T^{\text{meas}, \text{healthy}}(y)|. \end{aligned} \quad (28)$$

The corresponding simulations are shown in Figure 8.

As one can expect, increasing the number of data by considering more thermograms improves the reconstruction. This is visualized in Figure 9, where 50 thermograms for $\varepsilon_{\text{err}} = 0.06$ have been processed. Reconstructions now are much more satisfactory and they do not include spurious regions located far from the location of the true defect: only one defect is found, whose size, as expected, depends on the selected value of λ . In particular, when selecting $\lambda = 0.8$, the size and position in the $[0, L_y]$ interval are very sharp, although the correct depth and width of the defect are not found. We

also observe that the size of the reconstructed defect highly depends on the value of λ , being very easy to overestimate the size without having any a priori information. In the next section we will see that time-harmonic thermograms provide reconstructions that are much more robust with respect to λ .

We have repeated the experiment by increasing the number of thermograms to $N_{\text{lamps}} = 100$. In this case, the reconstruction is qualitatively equal as when $N_{\text{lamps}} = 50$, meaning that once a suitable number of steady thermograms has been processed, a further increase in the number of recorded thermograms does not produce better results. The corresponding figure is omitted for the sake of brevity. We have also tested the dependence of the reconstructions on the distance of the lamps to the plate. To do that, we have repeated the experiment in Figure 9 where lamps are located at points (s_x, s_y) with $s_x = -0.15$, by considering 50 positions with $s_x = -0.05$, i.e., by approximating the lamps to the side of the plate where thermograms are taken and then moving them away to $s_x = -0.45$. We observed that results are rather insensitive to the distance between the lamps and the plate for the considered locations, being slightly better when approximating the lamps.

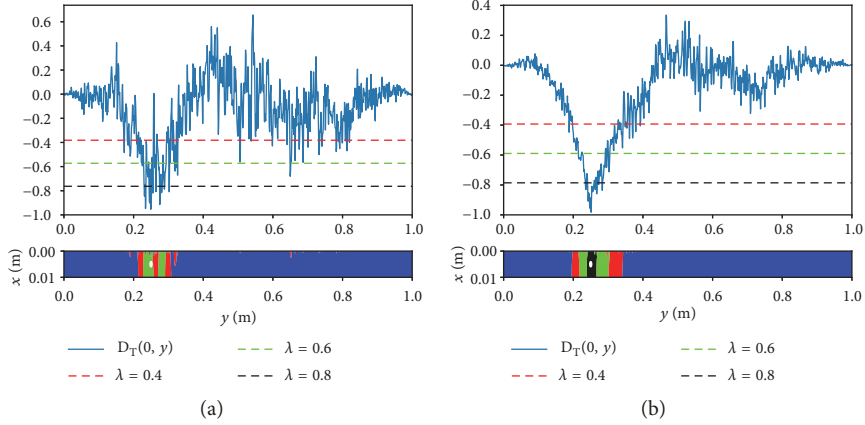


FIGURE 8: Counterpart of Figure 7(b) for a different set of ten thermograms. (a) Results for new thermograms for $\varepsilon_{\text{err}} = 0.06$. (b) Results for $\varepsilon = 0.015$.

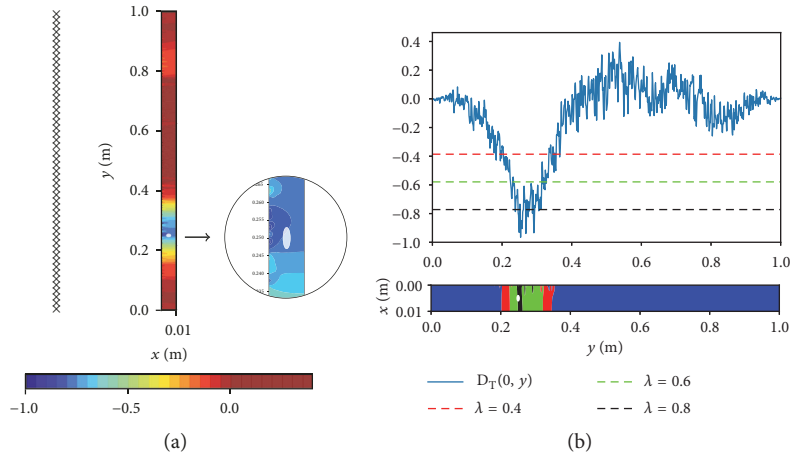


FIGURE 9: Counterpart of Figure 7 for $N_{\text{lamps}} = 50$.

To end this section, we consider a much more demanding situation, where the plate has three internal defects, with different shapes and sizes, and is located at different depths; see Figure 2(b). As one can expect, when dealing with high levels of noise (we take again $\varepsilon_{\text{err}} = 0.06$), individual topological derivatives corresponding to processing just a single thermogram do not provide satisfactory reconstructions, and, depending on the location of the lamp, some of the defects can be recovered, some of them can be completely disregarded, and, even worse, some spurious defects can be identified. This is illustrated in Figure 10.

By processing several thermograms, corresponding to different locations of the lamp, the problem is alleviated, but reconstructions are not satisfactory, as shown in Figure 11 which collects our results for $N_{\text{lamps}} = 50$ and $N_{\text{lamps}} = 100$ lamps uniformly distributed at the points $(-0.15, s_y)$ with $0 \leq s_y \leq 1$. It is remarkable that the most pronounced negative values of the topological derivative, i.e., when selecting $\lambda = 0.8$, gather around the defect centered at $(0.6L_x, 0.6L_y)$ even though it is smaller than the ellipsoid centered at $(0.5L_x, 0.25L_y)$ and further from the side $x = 0$ where thermograms are taken than the other two defects. We believe that this is due to the fact that it is located close to the middle

of the plate, and most of the thermograms contain relevant information about it.

The main conclusion of this section is that the steady topological derivative performs better than plain thermograms, but it is very sensitive to high levels of noise, providing poor approximations when dealing with challenging situations with several small defects. In the next section we will show that for those situations it is more convenient to consider time-harmonic excitations.

4.3. Time-Harmonic Thermograms. In this section we apply the topological derivative method to process thermograms in the time-harmonic case.

First, we inspected the plate with only one elliptical hole (see Figure 2(a)) by considering just one thermogram obtained by locating the lamp at $(-0.15, 0.5)$ and generating a time-harmonic excitation at $\omega = 1$ Hz. For the level of noise $\varepsilon_{\text{err}} = 0.01$, neither the thermogram (see Figure 4) nor the topological derivative (the figure is omitted for brevity) seem to contain any valuable information. As done for the steady case, we processed then several thermograms. We considered first 10 thermograms obtained by locating the lamp at different positions for the frequency $\omega = 1$ Hz. Results

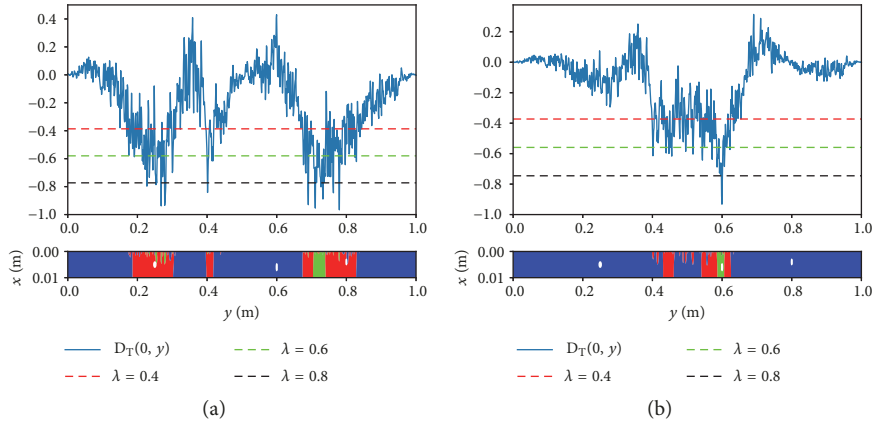


FIGURE 10: Topological derivative at $x = 0$ and reconstructed defects for different values of λ for the configuration with three defects. Only one thermogram is processed, associated with two different positions of the lamp. (a) Lamp located at $(-0.15, 0.5)$. (b) Lamp located at $(-0.15, 0.75)$.

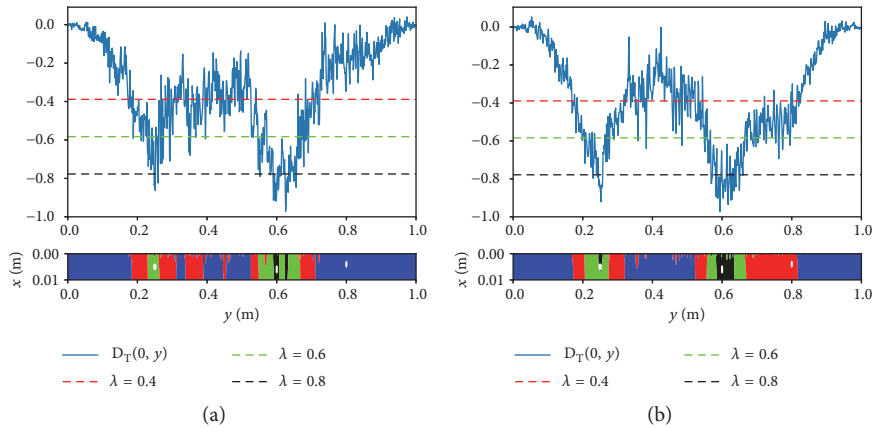


FIGURE 11: Counterpart of Figure 10 when processing N_{lamps} different thermograms associated with different positions of the lamp. (a) $N_{\text{lamps}} = 50$. (b) $N_{\text{lamps}} = 100$.

are shown in Figure 12, where, in particular, we observe in plot (a) that the most pronounced negative values of the topological derivative concentrate in a very small region near the location of the true defect. We obtain a very accurate estimation of the position and size of the defect, although the correct depth and width are not recovered and the defect seems to be located close to the side $x = 0$. Recall that, for the steady case, 10 thermograms were not enough since in some simulations we could obtain spurious defects; see Figure 7. Furthermore, the reconstruction is much more robust with respect to the selected value of λ in (27) than in the steady case (compare with Figure 9, which corresponds to 50 steady thermograms). Indeed, we see that there is not a very big difference between reconstructions for a really wide range of values of λ , and to generate spurious defects this constant has to take about $\lambda = 0.4$. By increasing the number of lamps to 50, this effect is amplified, but qualitatively, reconstructions are rather similar for $\lambda = 0.75$ and $\lambda = 0.5$ to those for only 10 lamps, as shown in Figure 13.

Next, we explored the combination of thermograms produced by considering different excitation frequencies. We generate 100 different thermograms by locating the lamp at

ten uniformly spaced positions and ten uniformly spaced frequencies between 0.8 Hz and 2 Hz. Results are presented in Figure 14. Again, we observe that the topological derivative attains a very acute minimum, which perfectly identifies the location of the hole. Indeed, the reconstructions are almost identical to those in Figure 13. By increasing the number of frequencies to $N_{\text{freq}} = 20$ and locating the lamp at $N_{\text{lamps}} = 20$ different positions, reconstructions are plot-indistinguishable to those in Figure 14, meaning that a further increase in the number of thermograms does not improve reconstructions. Indeed, by reducing the numbers to $N_{\text{lamps}} = 5$ and $N_{\text{freq}} = 5$, reconstructions are almost identical too.

To end this section, we illustrate the performance of the topological derivative for the configuration in Figure 2(b), where three holes of different sizes and shapes are present. As in the previous example, thermograms are highly polluted by noise when selecting $\epsilon_{\text{err}} = 0.01$. First we consider only the frequency $\omega = 1$ Hz and take 50 thermograms corresponding to different positions of the lamp. This provides the results in Figure 15, where we observe that the global minimum of the topological derivative is very acute and it occurs in a region very close to the location of the elliptical defect, which has the biggest area. This defect is the only one that is

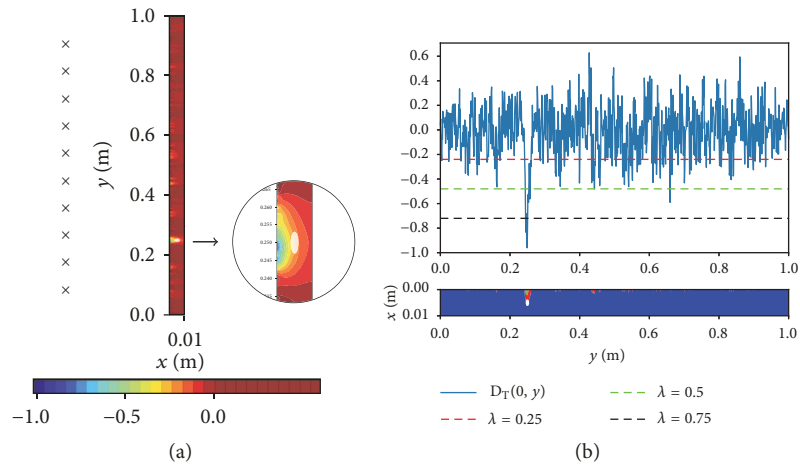


FIGURE 12: Results for time-harmonic thermograms for $\omega = 1$ Hz and the configuration with one defect. (a) Topological derivative for $N_{\text{lamps}} = 10$. (b) Topological derivative at $x = 0$ and reconstructed defects for several values of λ .

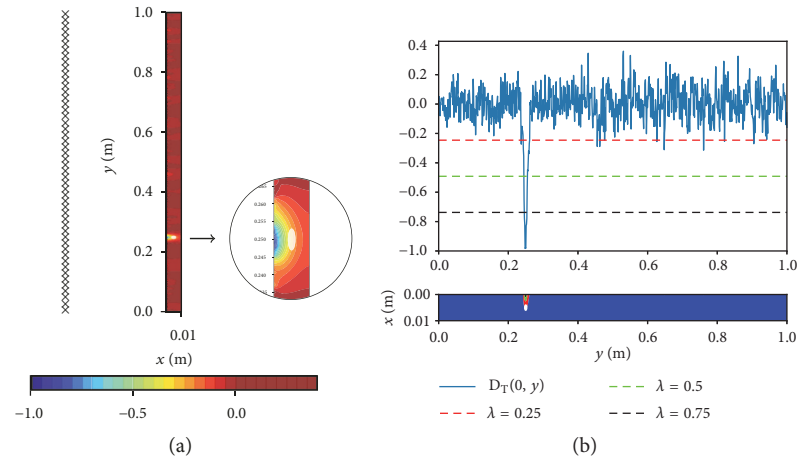


FIGURE 13: Results for $\omega = 1$ Hz when considering $N_{\text{lamps}} = 50$.

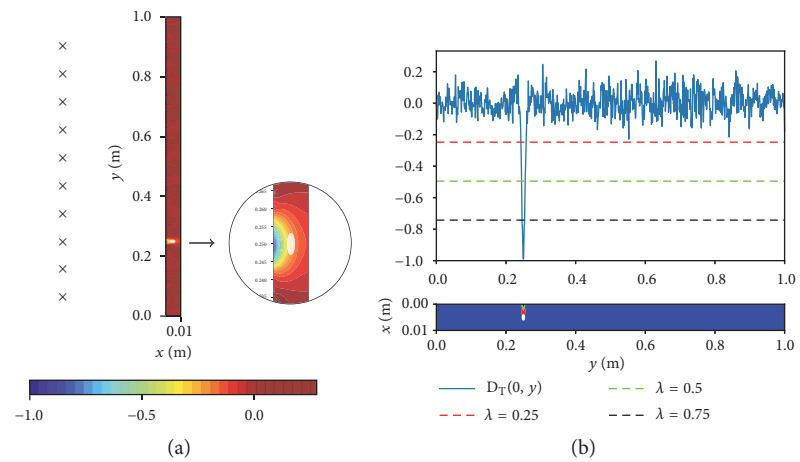


FIGURE 14: Results for $N_{\text{lamps}} = 10$ and $N_{\text{freq}} = 10$ uniformly distributed frequencies between 0.8 and 2 Hz.

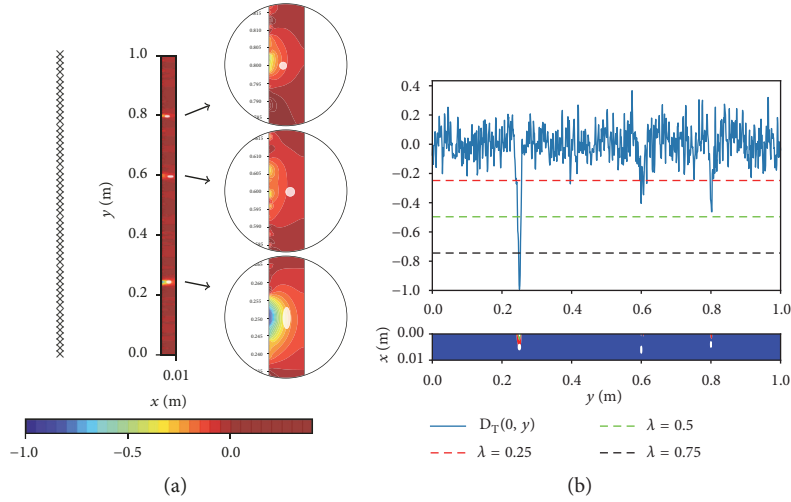


FIGURE 15: Results for the configuration with three defects when considering $N_{\text{lamps}} = 50$ time-harmonic excitations at the frequency $\omega = 1$ Hz.

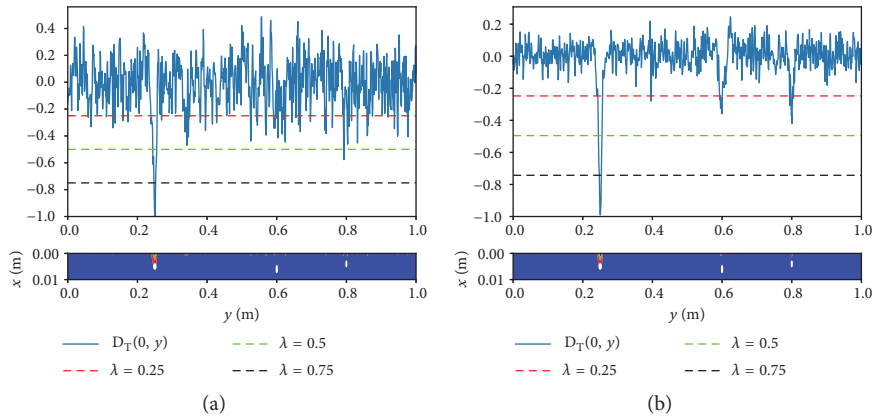


FIGURE 16: Counterpart of Figure 15(b) when considering a different number N_{lamps} of thermograms. (a) $N_{\text{lamps}} = 20$. (b) $N_{\text{lamps}} = 100$.

identified when selecting λ in (27) bigger than 0.5. The quality of the reconstruction of this defect is comparable to the reconstruction of the same defect in the plate with only one defect (compare with Figure 13). However, we also distinguish two local minima of the topological derivative that take place precisely in the regions close to the location of the remaining two defects. When selecting $\lambda = 0.25$, we recover the regions in red in Figure 15(b), which correspond to the true defects. If we reduce the number of thermograms to $N_{\text{lamps}} = 20$, then the two small circular holes are completely disregarded, while increasing the number to $N_{\text{lamps}} = 100$, reconstructions are almost the same as for $N_{\text{lamps}} = 50$, as can be observed in Figure 16. We have also checked that considering 10 locations of the lamp and 10 different frequencies, reconstructions are almost indistinguishable from those for 100 different locations of the lamp for only the frequency $\omega = 1$ Hz (not shown for brevity). However, considering $N_{\text{lamps}} = 20$ and $N_{\text{freq}} = 20$, reconstructions improve because the minima of the topological derivative become more acute and smooth, as can be observed in Figure 17. It is noticeable that the topological derivative captures slightly better the defect

centered at $(0.4L_x, 0.8L_y)$, whose radius is 1 mm, than the other circular defect, located at $(0.6L_x, 0.6L_y)$ with radius 1.25 mm. We believe that this is because the biggest one is located further from the size $x = 0$ of the plate, where the thermograms are taken.

4.4. Fluctuations in the Background Medium. In this section we will deal with an extremely demanding situation, where not only thermograms will be polluted by high levels of noise, but also the parameters of the medium and the defects (assumed to be known and constant in the previous section) will fluctuate now randomly. We will only consider time-harmonic simulations for the configuration with three defects.

As already mentioned, in all our previous simulations we selected the physical parameters for the plate corresponding to a standard aluminum alloy with constant values and to air for the defects. In this section we will allow these values to have random fluctuations around those constant values; i.e., we will generate our thermograms by solving the direct problem (8) by considering new parameters of

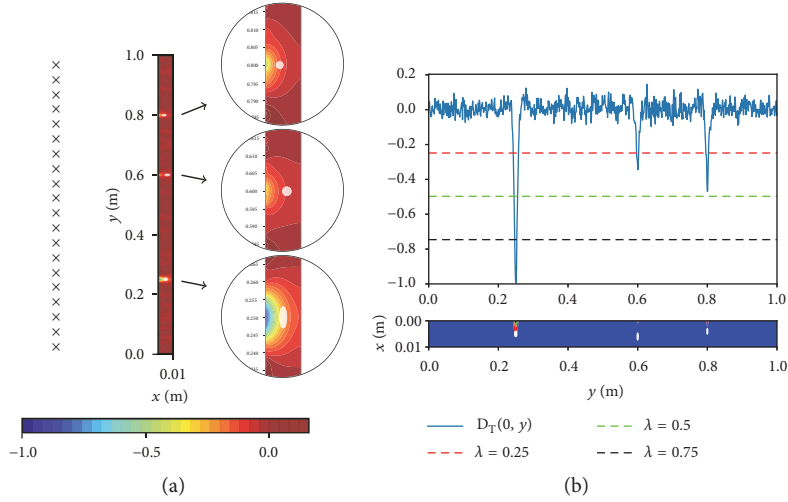


FIGURE 17: Results for the configuration with three defects when considering $N_{\text{lamps}} = 20$ and $N_{\text{freq}} = 20$.

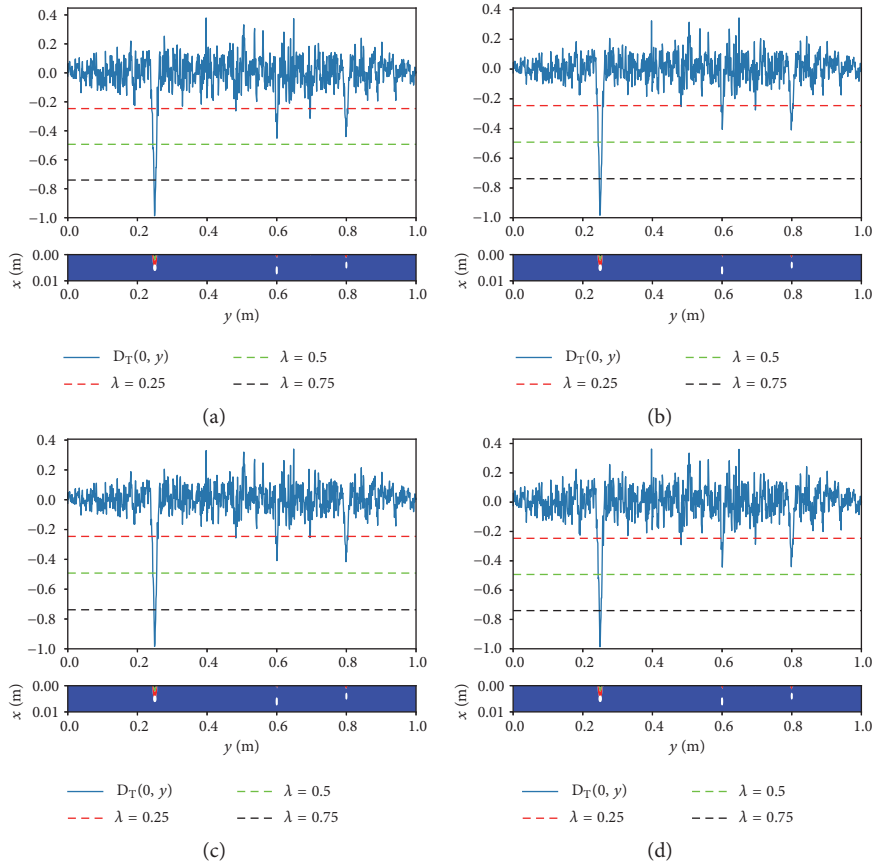


FIGURE 18: Topological derivative and reconstructed defects for parameter perturbations of size 10% when thermograms corresponding to $N_{\text{lamps}} = 5$ and $N_{\text{freq}} = 10$ are processed. (a) $(\eta_\kappa, \eta_\rho, \eta_c) = (0.1, 0, 0)$. (b) $(\eta_\kappa, \eta_\rho, \eta_c) = (0, 0.1, 0)$. (c) $(\eta_\kappa, \eta_\rho, \eta_c) = (0, 0, 0.1)$. (d) $(\eta_\kappa, \eta_\rho, \eta_c) = (0.1, 0.1, 0.1)$.

the form (3) with a perturbation η_μ with $|\eta_\mu(\mathbf{x})| \leq \varepsilon_\mu \mu(\mathbf{x})$, with $\mu = \rho, c$ or κ defined as the piecewise constant functions in (2). After computing the synthetic thermograms, we will pollute them by noise as in (22), for exactly the same demanding noise level $\varepsilon_{\text{err}} = 0.01$ considered in the previous section.

To implement the topological derivative (25) we consider the constant values κ_e , ρ_e , and c_e of standard aluminum, since one cannot assume to have knowledge about the true fluctuations present in the nonpure material.

First we consider random fluctuations of a 10% size. In all the plots in Figure 18 fifty thermograms are considered,

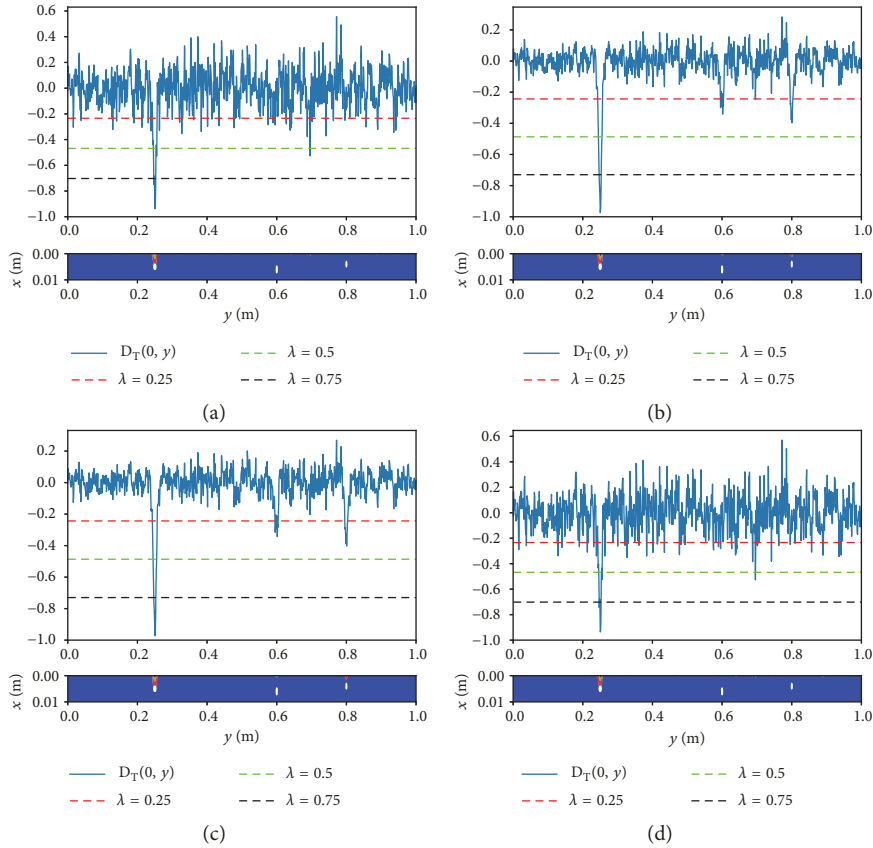


FIGURE 19: Topological derivative and reconstructed defects for parameter perturbations of size 20% when thermograms corresponding to $N_{\text{lamps}} = 10$ and $N_{\text{freq}} = 10$ are processed. (a) $(\eta_\kappa, \eta_\rho, \eta_c) = (0.2, 0, 0)$. (b) $(\eta_\kappa, \eta_\rho, \eta_c) = (0, 0.2, 0)$. (c) $(\eta_\kappa, \eta_\rho, \eta_c) = (0, 0, 0.2)$. (d) $(\eta_\kappa, \eta_\rho, \eta_c) = (0.2, 0.2, 0.2)$.

corresponding to $N_{\text{lamps}} = 5$ different positions of the lamp and to $N_{\text{freq}} = 10$ different frequencies ranging between 0.8 Hz and 2 Hz. We started by perturbing the conductivity κ by considering a random fluctuation $\eta_\kappa = 0.1$, obtaining the graph of the topological derivative at $x = 0$ and the associated reconstructions for different values of λ in (27) shown in Figure 18(a). Then, we varied the density ρ choosing $\eta_\rho = 0.1$ (Figure 18(b)) and the heat capacity c with $\eta_c = 0.1$ (Figure 18(c)), and, finally, we perturbed simultaneously the three parameters with $\eta_\kappa = 0.1$, $\eta_\rho = 0.1$, and $\eta_c = 0.1$ (Figure 18(d)). In all the situations, even when all the parameters are perturbed we were able to sharply identify the elliptical hole and to visualize the remaining small defects if λ is taken as $\lambda = 0.25$. This means that the method has no difficulties to deal with these levels of fluctuations, and, indeed, reconstructions are qualitatively identical to those corresponding to the same number of lamps and frequencies when no fluctuations are considered.

Increasing the level of fluctuation in κ to $\eta_\kappa = 0.2$ and increasing also the number of lamp positions to $N_{\text{lamps}} = 10$ while keeping $N_{\text{freq}} = 10$, we were only able to sharply recover the elliptical defect, while the small circular defects were completely disregarded (see Figure 19(a)). However, by either perturbing ρ with $\eta_\rho = 0.2$ or perturbing c with $\eta_c = 0.2$, we can identify the three defects as clearly as when those parameters are not altered, as shown in Figures 19(b) and 19(c).

Finally, as one can expect, when perturbing simultaneously the three parameters, only the biggest defect is identified (see Figure 19(d)). Keeping the same level of fluctuations but increasing the number of thermograms to 400 by considering $N_{\text{lamps}} = 20$ and $N_{\text{freq}} = 20$, the reconstructions associated with perturbations in the conductivity do not improve, while reconstructions associated with perturbations in the density and in the heat capacity become more clear due to more acute minima associated with the location of the three defects. This is shown in Figure 20.

Summing up, in this section we have checked that our time-harmonic topological derivative is extremely robust not only with respect to high noise levels in the measured thermograms, but also to perturbations in the media, being able to provide sharp reconstructions even in very demanding configurations with tiny defects and with fluctuations around a 10% in all the parameters and even with fluctuations about a 20% in the densities and heat capacities.

5. Conclusions

Throughout a wide gallery of numerical experiments, we have illustrated the ability of the topological derivative to process steady and time-harmonic thermograms for nondestructive testing of thin aluminum plates. We have shown that the topological derivative is a very powerful tool to postprocess

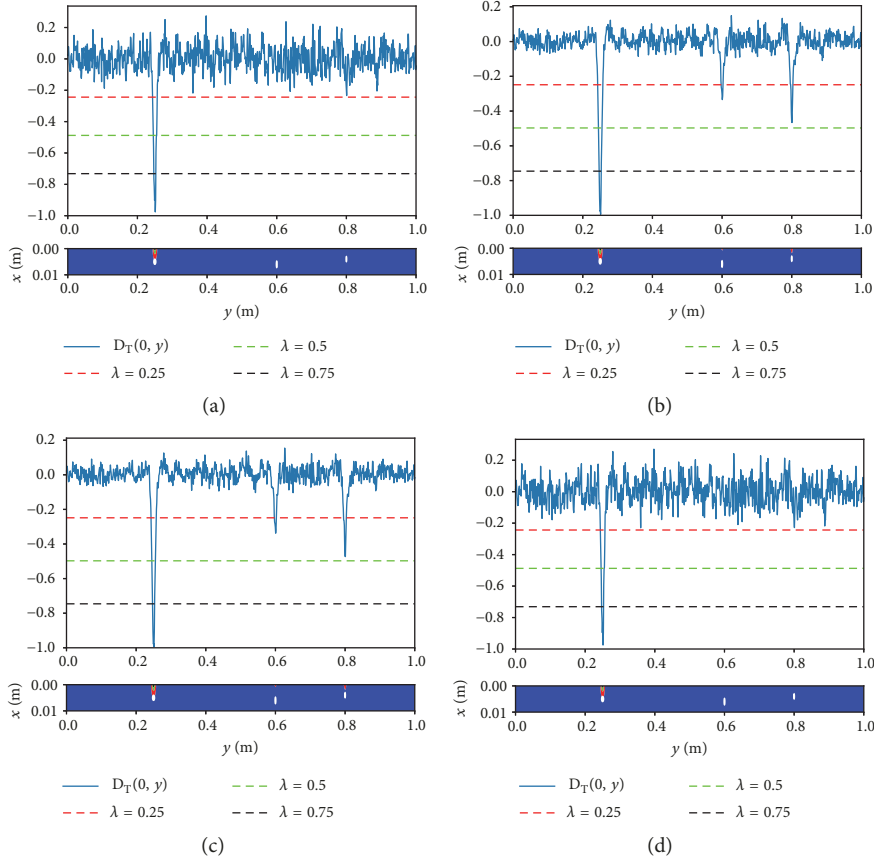


FIGURE 20: Counterpart of Figure 19 for $N_{\text{lamps}} = 20$ and $N_{\text{freq}} = 20$.

thermograms, even when those thermograms are highly corrupted by noise and at plain sight do not seem to contain relevant information about the presence of damage. From our numerical experiments, we conclude that it is much more recommendable to use time-harmonic thermograms than time-steady ones, since they are able to sharply recover the location in the y -direction and the approximate size of the true defects. The correct position in the x -direction and the width of the defects is not properly recovered. Furthermore, it is well known that this difficulty is inherent to this kind of problems, as reported in [43]. We want to empathise that for our applications this limitation is not a big deal, because the plates are very thin and the more relevant issue is to characterize the presence of damage and its approximate size and location (in the y -direction). Furthermore, in many applications, a plate is considered to be damaged if it contains some defects whose size is bigger than a critical one. This means that, in case of having one of those defects, it is completely irrelevant to find some other defects that are smaller than it. From this point of view, our method is very appealing. We believe that, using more general thermograms, corresponding to general transient heat excitations instead of steady or time-harmonic ones can improve reconstructions. This was tested in [14] for a two-dimensional heat problem in an unbounded media, where it was observed that time-harmonic data were not sufficient to find the true position of the buried defects, but general transient

measurements were suitable to find them. The extension to time-dependent excitations will be considered in future work.

On the other hand, we have further investigated the ability of topological derivatives to deal not only with noisy data, but also with noise in the physical parameters. We have seen that it is not very sensitive to them and provides reconstructions that are as sharp as when no fluctuations in the parameters are present for simultaneous fluctuations in the conductivity, density, and heat capacity around a 10%. Furthermore, in case of fluctuations in the densities and heat capacities, this level can be increased even to a 20%. Again, this feature makes the method very appealing for industrial applications since in practice one has always uncertainties about the exact values of the physical parameters.

Finally, we want to emphasize that we have explored the performance of a one-step method, which is rather fast to implement. Our reconstructions are not sharp, but they could be used as initial guesses for more sophisticated (and much more computational costly) iterative methods if sharp reconstructions of the defects in depth and width are desired. Some iterative methods that require suitable initial guesses are, for instance, shape derivative based algorithms [44, 45] and level set approaches [46, 47] or based on Tikhonov regularization, like the one presented in [43]. Another possibility could be to explore the use of second order topological derivatives [25, 48, 49], which would define an alternative

(and more computationally expensive than our strategy) one-step method which could provide better approximations.

Data Availability

The syntectic data used to support the findings of this study can be reproduced by solving the corresponding problems numerically, as indicated in the paper. They are also available from the corresponding author upon request

Conflicts of Interest

The authors declare that they have no conflicts of interest.

Acknowledgments

The authors are supported by the Spanish Ministry of Economy and Competitiveness under the Research Projects TRA2016-75075-R and MTM2017-84446-C2-1-R. We would like to thank M. Higuera, J.M. Perales, and J.M. Vega for fruitful discussions.

References

- [1] G. Gaussorgues, *Infrared Thermography*, Springer, Berlin/Heidelberg, Germany, 1994.
- [2] J. T. Costello, C. D. McInerney, C. M. Bleakley, J. Selfe, and A. E. Donnelly, "The use of thermal imaging in assessing skin temperature following cryotherapy: a review," *Journal of Thermal Biology*, vol. 37, no. 2, pp. 103–110, 2012.
- [3] M. Moghbel and S. Mashohor, "A review of computer assisted detection/diagnosis (CAD) in breast thermography for breast cancer detection," *Artificial Intelligence Review*, vol. 39, no. 4, pp. 305–313, 2013.
- [4] K. E. Cramer, P. A. Howell, and H. I. Syed, "Quantitative thermal imaging of aircraft structures," *Proc. SPIE Thermosense XVII*, vol. 2473, pp. 226–232, 1995.
- [5] H. I. Syed, W. Winfree, E. Cramer, and P. A. Howell, "Thermographic detection of corrosion in aircraft skin," *Review of progress in quantitative nondestructive evaluation*, pp. 2035–2041, 1993.
- [6] A. Kylili, P. A. Fokaides, P. Christou, and S. A. Kalogirou, "Infrared thermography (IRT) applications for building diagnostics: A review," *Applied Energy*, vol. 134, pp. 531–549, 2014.
- [7] <http://www.flir.co.uk>.
- [8] C. Meola, *Infrared thermography: Recent advances and future trends*, Bentham Science, New York, NY, USA, 2012.
- [9] M. Rojczyk, H. R. Orlande, M. . Colaço et al., "Inverse heat transfer problems: an application to bioheat transfer," *Computer Assisted Methods in Engineering and Science*, vol. 22, no. 4, pp. 365–383, 2015.
- [10] D. C. Knupp, C. P. Naveira-Cotta, J. . Ayres, H. R. Orlande, and R. M. Cotta, "Space-variable thermophysical properties identification in nanocomposites via integral transforms, Bayesian inference and infrared thermography," *Inverse Problems in Science and Engineering*, vol. 20, no. 5, pp. 609–637, 2012.
- [11] L. F. Saker, H. R. Orlande, C.-H. Huang, G. H. Kanevce, and L. P. Kanevce, "Simultaneous estimation of the spacewise and timewise variations of mass and heat transfer coefficients in drying," *Inverse Problems in Science and Engineering*, vol. 15, no. 2, pp. 137–150, 2007.
- [12] R. Gade and T. B. Moeslund, "Thermal cameras and applications: a survey," *Machine Vision and Applications*, vol. 25, no. 1, pp. 245–262, 2014.
- [13] R. Usamentiaga, P. Venegas, J. Guerediaga, L. Vega, J. Molleda, and F. G. Bulnes, "Infrared thermography for temperature measurement and non-destructive testing," *Sensors*, vol. 14, no. 7, pp. 12305–12348, 2014.
- [14] A. Carpio and M.-L. Rapún, "Domain reconstruction using photothermal techniques," *Journal of Computational Physics*, vol. 227, no. 17, pp. 8083–8106, 2008.
- [15] A. Carpio and M.-L. Rapún, "Parameter identification in photothermal imaging," *Journal of Mathematical Imaging and Vision*, vol. 49, no. 2, pp. 273–288, 2014.
- [16] M. Pena and M.-L. Rapún, "Damage detection in two-dimensional plates via infrared thermography," in *Proceedings of ECCM6/ECFD7*, Glasgow, June 2018, <http://www.eccm-ecfd2018.org/admin/files/filePaper/p1317.pdf>.
- [17] S. Amstutz, "Sensitivity analysis with respect to a local perturbation of the material property," *Asymptotic Analysis*, vol. 49, no. 1-2, pp. 87–108, 2006.
- [18] A. Carpio and M.-L. Rapún, "Hybrid topological derivative and gradient-based methods for electrical impedance tomography," *Inverse Problems*, vol. 28, no. 9, 095010, 22 pages, 2012.
- [19] S. Chaabane, M. Masmoudi, and H. Meftahi, "Topological and shape gradient strategy for solving geometrical inverse problems," *Journal of Mathematical Analysis and Applications*, vol. 400, no. 2, pp. 724–742, 2013.
- [20] S. M. Giusti, A. A. Novotny, and J. Sokolowski, "Topological derivative for steady-state orthotropic heat diffusion problem," *Structural and Multidisciplinary Optimization*, vol. 40, no. 1-6, pp. 53–64, 2010.
- [21] A. A. Novotny and V. Sales, "Energy change to insertion of inclusions associated with a diffusive/convective steady-state heat conduction problem," *Mathematical Methods in the Applied Sciences*, vol. 39, no. 5, pp. 1233–1240, 2016.
- [22] P. Gangl, S. Amstutz, and U. Langer, "Topology Optimization of Electric Motor Using Topological Derivative for Nonlinear Magnetostatics," *IEEE Transactions on Magnetics*, vol. 52, no. 3, pp. 1–4, 2016.
- [23] A. A. Novotny, J. Sokolowski, and A. Żochowski, "Topological Derivatives of Shape Functionals. Part I: Theory in Singularly Perturbed Geometrical Domains," *Journal of Optimization Theory and Applications*, 2018.
- [24] A. A. Novotny, J. Sokolowski, and A. Żochowski, "Topological Derivatives of Shape Functionals. Part II: First-Order Method and Applications," *Journal of Optimization Theory and Applications*, 2018.
- [25] A. A. Novotny, J. Sokolowski, and A. Żochowski, "Topological Derivatives of Shape Functionals. Part III: Second-Order Method and Applications," *Journal of Optimization Theory and Applications*, 2018.
- [26] A. A. Novotny and J. Sokolowski, *Topological derivatives in shape optimization*, Interaction of Mechanics and Mathematics, Springer, Heidelberg, Berlin, 2013.
- [27] A. Wahab, "Stability and resolution analysis of topological derivative based localization of small electromagnetic inclusions," *SIAM Journal on Imaging Sciences*, vol. 8, no. 3, pp. 1687–1717, 2015.

- [28] A. Wahab, T. Abbas, N. Ahmed, and Q. M. Zia, "Detection of electromagnetic inclusions using topological sensitivity," *Journal of Computational Mathematics*, vol. 35, no. 5, pp. 642–671, 2017.
- [29] H. Ammari, J. Garnier, V. Jugnon, and H. Kang, "Stability and resolution analysis for a topological derivative based imaging functional," *SIAM Journal on Control and Optimization*, vol. 50, no. 1, pp. 48–76, 2012.
- [30] J. Sokolowski and A. Zochowski, "On the topological derivative in shape optimization," *SIAM Journal on Control and Optimization*, vol. 37, no. 4, pp. 1251–1272, 1999.
- [31] A. A. Novotny, R. A. Feijoo, E. Taroco, and C. Padra, "Topological sensitivity analysis," *Computer Methods Applied Mechanics and Engineering*, vol. 192, no. 7-8, pp. 803–829, 2003.
- [32] A. Carpio and M.-L. Rapún, "Solving inhomogeneous inverse problems by topological derivative methods," *Inverse Problems*, vol. 24, no. 4, Article ID 045014, 2008.
- [33] A. Carpio and M. L. Rapún, "Topological derivatives for shape reconstruction," in *Inverse Problems and Imaging*, vol. 1943 of *Lecture Notes in Math.*, pp. 85–133, Springer, Berlin, 2008.
- [34] C. Y. Ahn, K. Jeon, Y.-K. Ma, and W.-K. Park, "A study on the topological derivative-based imaging of thin electromagnetic inhomogeneities in limited-aperture problems," *Inverse Problems*, vol. 30, no. 10, Article ID 105004, 2014.
- [35] W.-K. Park, "Multi-frequency topological derivative for approximate shape acquisition of curve-like thin electromagnetic inhomogeneities," *Journal of Mathematical Analysis and Applications*, vol. 404, no. 2, pp. 501–518, 2013.
- [36] J. F. Funes, J. M. Perales, M.-L. Rapún, and J. M. Vega, "Defect detection from multi-frequency limited data via topological sensitivity," *Journal of Mathematical Imaging and Vision*, vol. 55, no. 1, pp. 19–35, 2016.
- [37] R. Griesmaier, "Multi-frequency orthogonality sampling for inverse obstacle scattering problems," *Inverse Problems*, vol. 27, no. 8, 085005, 23 pages, 2011.
- [38] S. Hou, K. Huang, K. Solna, and H. Zhao, "A phase and space coherent direct imaging method," *The Journal of the Acoustical Society of America*, vol. 125, no. 1, pp. 227–238, 2009.
- [39] Y.-D. Joh and W.-K. Park, "Analysis of multi-frequency subspace migration weighted by natural logarithmic function for fast imaging of two-dimensional thin, arc-like electromagnetic inhomogeneities," *Computers & Mathematics with Applications*, vol. 68, no. 12, pp. 1892–1904, 2014.
- [40] W. Park, "Non-iterative imaging of thin electromagnetic inclusions from multi-frequency response matrix," *Progress in Electromagnetics Research*, vol. 106, pp. 225–241, 2010.
- [41] R. Potthast, "A study on orthogonality sampling," *Inverse Problems*, vol. 26, no. 7, p. 074015, 2010.
- [42] F. Hecht, "New development in freefem++," *Journal of Numerical Mathematics*, vol. 20, no. 3-4, pp. 251–265, 2012.
- [43] N. T. Thành, H. Sahli, and D. N. Hào, "Detection and characterization of buried landmines using infrared thermography," *Inverse Problems in Science and Engineering*, vol. 19, no. 3, pp. 281–307, 2011.
- [44] I. Cimrak, "Inverse thermal imaging in materials with nonlinear conductivity by material and shape derivative method," *Mathematical Methods in the Applied Sciences*, vol. 34, no. 18, pp. 2303–2317, 2011.
- [45] F. Caubet, C. Conca, and M. Godoy, "On the detection of several obstacles in 2D Stokes flow: topological sensitivity and combination with shape derivatives," *Inverse Problems and Imaging*, vol. 10, no. 2, pp. 327–367, 2016.
- [46] K. Ito, K. Kunisch, and Z. Li, "Level-set function approach to an inverse interface problem," *Inverse Problems*, vol. 17, no. 5, pp. 1225–1242, 2001.
- [47] S. Osher and R. Fedkiw, *Level Set Methods and Dynamic Implicit Surfaces*, vol. 153, Springer, New York, NY, USA, 2003.
- [48] J. Rocha de Faria, A. A. Novotny, R. A. Feijóo, and E. Taroco, "First- and second-order topological sensitivity analysis for inclusions," *Inverse Problems in Science and Engineering*, vol. 17, no. 5, pp. 665–679, 2009.
- [49] M. Hintermüller, A. Laurain, and A. A. Novotny, "Second-order topological expansion for electrical impedance tomography," *Advances in Computational Mathematics*, vol. 36, no. 2, pp. 235–265, 2012.



Hindawi

Submit your manuscripts at
www.hindawi.com

